Acta Materialia 263 (2024) 119531

Contents lists available at ScienceDirect

Acta Materialia

journal homepage: www.elsevier.com/locate/actamat

# Effect of compositional heterogeneity on the mechanical properties of a single-phase Cu-9Al alloy with different grain sizes

H. Wang [a], B.S. Dong [a,b], Z.B. Chen [a,c], J.Q. Liu [a], N. Haghdadi [d], R.Q. Lu [a], S. Primig [d], Z.Y. Wang [e], Z.X. Pan [b], H.J. Li [b,*], S.P. Ringer [a,*], X.Z. Liao [a,*]

[a] Australian Centre for Microscopy & Microanalysis, and School of Aerospace, Mechanical and Mechatronic Engineering, The University of Sydney, Sydney, NSW 2006, Australia
[b] School of Mechanical, Materials, Mechatronic and Biomedical Engineering, University of Wollongong, Wollongong NSW 2522, Australia
[c] Research Institute for Advanced Manufacturing, Department of Industrial and Systems Engineering, The Hong Kong Polytechnic University, Hong Kong, China
[d] School of Materials Science & Engineering, UNSW Sydney, NSW 2052, Australia
[e] Australian Nuclear Science and Technology Organisation (ANSTO), Sydney, NSW, 2234, Australia

ARTICLE INFO

*Keywords:*
Compositional heterogeneity, mechanical properties, cu-al alloys, additive manufacturing

ABSTRACT

Recent investigations have indicated that compositional heterogeneity, which is compositional undulation of alloying elements in single-phase solid solutions, can enhance the strength without sacrificing ductility, similar to cluster strengthening, of single-crystal nano-pillars and bulk nanocrystalline metallic materials. However, the impact of compositional heterogeneity on the mechanical properties of coarse-grained metallic materials is not yet fully understood. In this study, we examine the influence of compositional heterogeneity on the tensile mechanical properties of a Cu-9Al (at.%) alloy with a coarse-grained structure fabricated using wire arc additive manufacturing and with an ultrafine-grained structure after further processing. Our results demonstrate that the effects of compositional heterogeneity depend significantly on the grain size. Specifically, in ultrafine-grained samples, there is a remarkable improvement in strength with only a slight reduction in ductility. However, as grain size increases, the strengthening effect of compositional heterogeneity diminishes, resulting in softening with a significant loss of ductility. These phenomena can be attributed to the behaviour of dislocations in the materials. Overall, this study highlights the importance of understanding the relationship between compositional heterogeneity, grain size, and mechanical properties in metallic materials, which can inform the design of new materials with improved strength and ductility.

## 1. Introduction

It is well known that metallic materials can be strengthened by grain refinement, work hardening, precipitation, and solid solution strengthening. Recent investigations revealed that compositional heterogeneity presents a similar strengthening effect as cluster strengthening [1,2], which enhances the strength without sacrificing the ductility of materials [3–8]. Most recent studies focused on investigating the effect of compositional heterogeneity in multiple-principal-element alloys or high-entropy alloys [4,5,8–12]. Experimental and theoretical results suggest that the increasing degree of compositional heterogeneity can overcome the strength–ductility trade-off and enhance the fatigue performance of bulk materials [3,8]. The underlying mechanisms are dislocation interactions and tangling, which are enhanced by compositional heterogeneities [3,5,9]. However, uncertainties remain in the detailed role of compositional heterogeneity on properties. For example, the alloy systems studied so far usually contained at least three alloying elements [4,5,8–11]. This has made it challenging to clarify how an individual alloying element contributes to the degree of local compositional heterogeneity. Further, it remains unknown if the reported sluggish dislocation slip in multiple-principal-element alloys is caused by the large lattice distortion [13] or by compositional heterogeneities. Meanwhile, most mechanical tests were conducted on either nanocrystalline materials [3,5] or single crystal nano-pillars [9,10]. Little evidence has been provided on whether this strengthening mechanism can be applied to coarse-grained (CG) binary polycrystalline materials. For nanocrystalline materials, the low work hardening rate and minimal dislocation accumulation limit their ductility [12–15]. In

* Corresponding authors.
*E-mail addresses:* huijun@uow.edu.au (H.J. Li), simon.ringer@sydney.edu.au (S.P. Ringer), xiaozhou.liao@sydney.edu.au (X.Z. Liao).

https://doi.org/10.1016/j.actamat.2023.119531
Received 11 June 2023; Received in revised form 15 October 2023; Accepted 12 November 2023
Available online 13 November 2023
1359-6454/© 2023 The Authors. Published by Elsevier Ltd on behalf of Acta Materialia Inc. This is an open access article under the CC BY license (http://creativecommons.org/licenses/by/4.0/).

contrast, there is sufficient room for dislocation accumulation inside of the grains of CG materials. To investigate this further, we studied a binary single-phase face-centred cubic (FCC) Cu-9Al (at.%) solid solution alloy. This alloy is free of precipitation of any secondary phase, ensuring that only one variable determining tensile strength and ductility will be systematically changed in this study.

Wire arc additive manufacturing (WAAM) was used to fabricate the Cu-9Al alloy. Additive manufacturing of metallic materials offers distinct advantages over traditional manufacturing techniques, which include design freedom, less tooling requirements, near net or net shape production, efficient use of materials, short lead time, and substantial cost savings in many cases [14,15]. It can also be utilized to manufacture some alloys that would otherwise be impossible to produce using traditional metallurgical methods [16]. Due to the feasibility of economically producing large-scale metal components with relatively high deposition rates by WAAM, significant progress has been made in advancing the understanding of this process [17]. Cu and Al wires were used as the raw materials for the fabrication without pre-alloying. The manufacturing process does not allow sufficient time for homogenization [18–21], resulting in compositional heterogeneity in the as-fabricated parts. Elemental segregation/partitioning is frequently observed in additively manufactured metallic materials where alloying elements segregate on cellular structures [22] or partition to form a secondary phase [23]. On the contrary, compositional heterogeneity refers to the compositional undulation of alloying elements in a single-phase solid solution alloying system. Different from an energetically favoured solute clustering [1,2,24], compositional heterogeneity is usually a non-equilibrium high-energy state, which can be eliminated via heat treatment. In this study, we conducted a systematic investigation to explore the degree of compositional heterogeneity in Cu-9Al alloy fabricated by WAAM and its impact on mechanical properties as a function of grain size.

## 2. Experimental procedures

The WAAM Cu-9Al (at.%) samples were fabricated using a Kemppi Master Tungsten Inert gas MLS 2000 with 160 A current and 3.5 mm arc length [25]. Two wire-feed nozzles were used for printing. The wires used were a 99.9 wt.% purity copper (Cu) wire and a 99.8 wt.% purity aluminium (Al) wire, both with an outside diameter of 0.9 mm. Independent wire-feed controls were applied to the system, which allowed adjustment of the chemical composition of the resulting alloy during the deposition process. The Cu and Al wires were fed at rates of 1300 and 311 mm/min, respectively. The deposition energy was kept at 20.2 kJ/g to ensure the stability of the deposition. The scanning speed was 95 mm/min. The pre-heating temperature of the substrate was set to 400 °C. High-purity Ar gas was continuously purged into the build chamber throughout the process.

Three bar-shaped samples with a dimensions of 30 × 7 × 4 $mm^3$ and six dog-bone samples with gauge dimensions of 10 × 2 × 1.5 $mm^3$ were extracted from each build-up wall (100 × 45 × 7 $mm^3$), as shown in Fig. 1. Samples were obtained at least 5 mm away from the top surface of the build-up wall and 8 mm away from the substrate to exclude the top and bottom volumes that would have distinct microstructural differences. Six types of samples with different microstructures were prepared. These comprise non-homogenized as-fabricated (NH-AF), homogenized as-fabricated (H-AF), non-homogenized–cold rolled (NH-CR), homogenized–cold rolled (H-CR), non-homogenized–recrystallized (NH-R), and homogenized– recrystallized (H-R) Cu-9Al samples. Their processing conditions are listed in Table 1. The samples after the homogeneous annealing process were cooled with the furnace. The recrystallization process was set at 600 °C for 1 hour, and water quenching was employed to prevent grain growth.

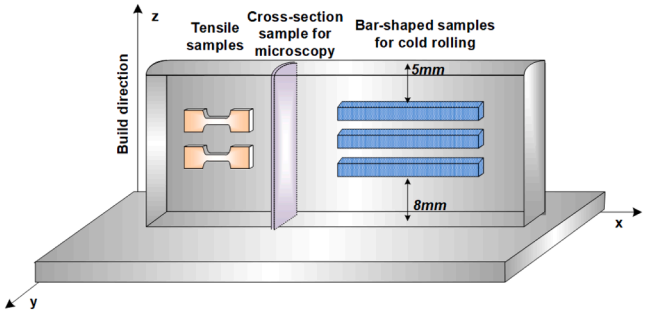


**Fig. 1.** Schematic diagram demonstrating how samples were extracted from the as-printed build.

Specimens for electron backscatter diffraction (EBSD) characterization were cut using an Acctom-50 diamond saw, ground using diamond lapping films with diamond grain sizes of 30, 15, 6, 3, and 1 μm and then polished using 0.05 μm oxide dispersion suspension. Specimens for transmission electron microscopy (TEM) investigation were sliced and ground to a thickness of ~ 60 μm, followed by ion milling using a Gatan model 691 precision ion polishing system at –50 °C, beam voltage of 4 kV and milling angle of ± 6° Needle-shaped specimens for atom probe tomography (APT) were prepared using a standard 2-stage electropolishing process with universal electrolytes [26].

EBSD experiments were conducted using a Zeiss Ultra scanning electron microscope (SEM) equipped with an EBSD detector and an X-ray energy dispersive spectroscopy (EDS) detector working at 20 kV. EBSD maps were acquired with a step size of 25 nm. The spatial resolution of the EBSD technique is limited by the acceleration voltage of the incident electron beam and the atomic number of the sample, which is of the order of 30 nm [27]. Scanning transmission electron microscopy (STEM) characterization was performed using a Titan Themis-Z double-corrected microscope equipped with ChemiSTEM (Super-X) EDS detectors and a Gatan Quantum ER/965 GIF dual EELS system working at 300 kV. All compositional mappings were conducted under a beam current of 200 pA and sufficiently long data collection times to ensure > 100,000 counts to minimise statistical errors. Electron energy loss spectroscopy (EELS) thickness mapping was conducted in the TEM mode to evaluate local specimen thickness. The formula used for the thickness measurements was $t = \lambda \ln(I_t / I_0)$, where $t$ is the specimen thickness, $\lambda$ is the mean free path of inelastic electron scattering with a value of 78 nm [28], and $I_t$ and $I_0$ are the total and zero-loss intensities in the electron energy-loss spectrum, respectively [29].

A semi-convergence angle of 25.1 mrad was used to acquire atomic resolution images. STEM bright-field (BF) images were collected in the (semi-) angle range of 0–10 mrad. The STEM high-angle annual dark-field (HAADF) images were obtained with a collection angle of 76–200 mrad (camera length of 73 mm) [30]. A beam current of 50 pA, a dwell time of 10 μs per pixel and an image size of 1024 × 1024 pixel were utilized. An FEI DF4 detector was used for STEM differential phase contrast imaging to explore the variation of the local electrostatic potential field of the samples with a collection angle range of 9–51 mrad (camera length of 230 mm). Differential phase contrast maps are acquired based on the differential of the phase shift [31] and reconstructed using the Thermo Scientific Velox software.

APT experiments were carried out in a laser-assisted CAMECA local electrode atom probe (LEAP) 4000X Si at a cryogenic temperature of

**Table 1**
Sample processing conditions.

| Sample | Processing condition |
|---|---|
| NH-AF | WAAM |
| H-AF | NH-AF + annealing at 900 °C for 48 h |
| NH-CR | NH-AF + cold rolling to 50 % thickness reduction |
| H-CR | H-AF + cold rolling to 50 % thickness reduction |
| NH-R | NH-CR + annealing at 600 °C for 1 h |
| H-R | H-CR + annealing at 600 °C for 1 h |

~50 K with a 90 mm straight flight path, and a pulse frequency of ~200 kHz. The tomographic reconstruction was performed using CAMECA's Integrated Visualization & Analysis Software version 3.8.4. Tip radius was derived from the voltage evolution method. The default image compression factor (1.65), and $k_f$ (3.30) were applied.

At least three tensile tests were conducted on each type of samples. The tests were conducted using an MTS 370 hydraulic load unit at a constant strain rate of $5 \times 10^{-3}\ s^{-1}$ at room temperature. The gauge volume of the tensile specimens was $10 \times 2 \times 1.5\ mm^3$. An extensometer was used to measure the strain during the tensile deformation. Loading–unloading–reloading (LUR) tensile tests were conducted at room temperature. Eight loading–unloading cycles were conducted during each tensile test. Upon straining to a designated strain (i.e., 2 %) at a strain rate of $5 \times 10^{-4}\ s^{-1}$, the specimen was unloaded by the stress-control mode to 20 N at the unloading rate of 200 $N{\cdot}min^{-1}$, followed by reloading at a strain rate of $5 \times 10^{-4}\ s^{-1}$ to the same applied stress before the next unloading.

In-situ compression tests of micropillars were performed using a Hysitron PI-85 picoindenter in the displacement-control mode with a displacement rate of 5 nm/s or a strain rate of $\sim 5 \times 10^{-3}\ s^{-1}$. Single-crystalline micropillars were prepared using a focused ion beam. The pillars were prepared in such a way that the compression direction is along a ⟨100⟩ direction and the electron beam direction is parallel to a ⟨011⟩ direction. All the pillars had similar dimensions of ~ 1 μm in diameter at the pillar top, ~ 3 μm in length, and ~3° tapering angle. At least three tests were conducted on each type of samples. A total displacement of 900 nm was performed, resulting in an engineering strain of 30%. It is expected that a large aspect ratio of length to diameter increases significantly the possibility of buckling while a small ratio results in unrealistic extra strain hardening [32]. Therefore, pillars with aspect ratios ranging 1:2 – 1:3 are recommended for micro-compression tests [32].

## 3. Results

### 3.1. Mechanical properties

Typical engineering stress–strain curves of the six types of samples are plotted in Fig. 2a. Mechanical properties extracted from the stress–strain curves are listed in Table 2. Compositional heterogeneity clearly changes the tensile behaviour of the different types of samples. Compared to the NH-AF samples, the H-AF samples present simultaneous improvement in ultimate tensile strength (UTS) and ductility, indicating that compositional heterogeneity is detrimental to the mechanical properties of the as-fabricated state. Compositional heterogeneity leads to 4.6 % higher yielding strength (YS) (from 693 MPa to 725 MPa) and 4.5 % higher UTS (from 713 MPa to 745 MPa) with ~3 % (from 15% to 12%) reduction in ductility in the CR samples. It only presents similar YS and slightly higher UTS (~3 %) but significantly reduces the ductility by ~16 % (57% vs 73 %) in the R samples. As the ductility improvement is the most substantial in R samples after homogenization (16 %), the work-hardening rates of NH-R and H-R samples are studied further. The results of the NH-R and H-R samples are presented in Fig. 2b with red and blue colours, respectively. At a true strain level of ~0.01, the NH-R sample presents a transient hardening, with the inflection point denoted by the black arrow. Prior to the inflection point, the work-hardening rate of the NH-R sample is lower than that of the H-R sample. However, beyond the 0.01 true strain level, the NH-R sample experienced a burst of work hardening, surpassing that of the H-R sample.

**Table 2**
Tensile mechanical properties of the samples studied. Average grain size (d), YS, UTS, and ductility (%) are included.

| | | Nonhomogenized | Homogenized |
|---|---|---|---|
| **AF ($d = 840$ μm)** | **YS (MPa)** | 87 ± 2 | 76 ± 5 |
| | **UTS (MPa)** | 253 ± 10 | 259 ± 12 |
| | **Ductility (%)** | 69 ± 4 | 76 ± 6 |
| **CR ($d = 300$ nm)** | **YS (MPa)** | 725 ± 7 | 693 ± 9 |
| | **UTS (MPa)** | 745 ± 7 | 713 ± 16 |
| | **Ductility (%)** | 12 ± 0 | 15 ± 1 |
| **R ($d = 24$ μm)** | **YS (MPa)** | 175 ± 7 | 174 ± 2 |
| | **UTS (MPa)** | 430 ± 8 | 417 ± 9 |
| | **Ductility (%)** | 57 ± 7 | 73 ± 2 |

### 3.2. Microstructures and composition in as-fabricated and cold-rolled samples

Fig. 3a presents an EBSD inverse pole figure (IPF) map of an NH-AF sample, revealing an average grain size of 840 mm ± 100 mm. SEM-EDS elemental mapping of Cu and Al elements is shown in Fig. 3b. Based on literature reports, the spatial resolution of our EDS experimental setup for Cu should be ~ 1 μm [33]. The EDS maps demonstrate a relatively uniform distribution of Cu (91.17 ± 0.02 at.%) and Al (8.83 ± 0.02 at. %) in relation to the low spatial resolution. Fig. 3c presents an EBSD IPF map taken from an NH-CR sample, two types of microstructures are observed in this sample, which are twinned areas and shear banding areas. 60°/<111> twin boundaries (TBs) are indicated by red lines. These twins are assumed to be deformation twins due to the severe plastic deformation of the sample and the relatively thin twin thickness (~ 250 nm). The average grain size of the twinned areas is 1.13 ± 0.20 μm (including TBs). Smaller grains with an average grain size of 290 ± 120 nm are observed in shear bands. Fig. 3d presents an EBSD IPF map

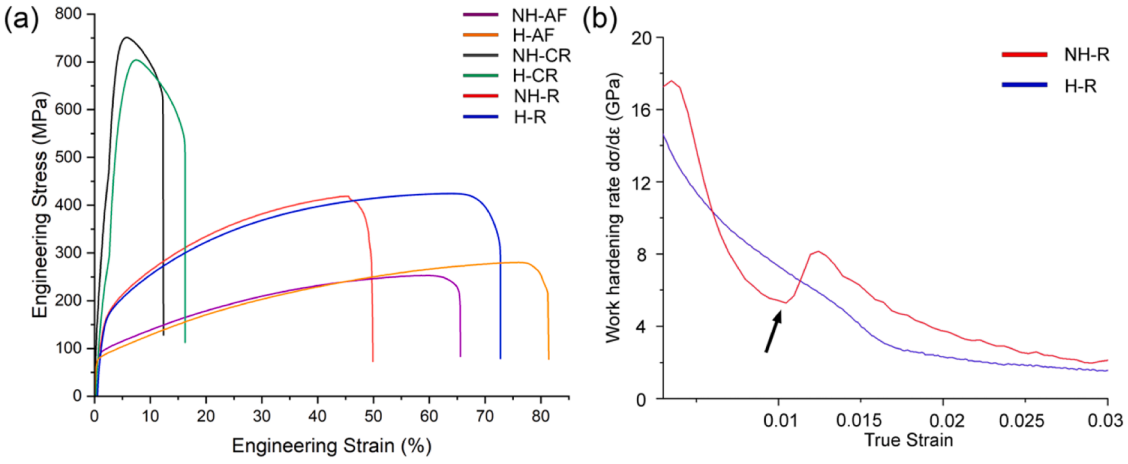


**Fig. 2.** (a) Typical engineering tensile stress–strain curves of the six types of samples. (b) Strain hardening rates of NH-R and H-R samples.

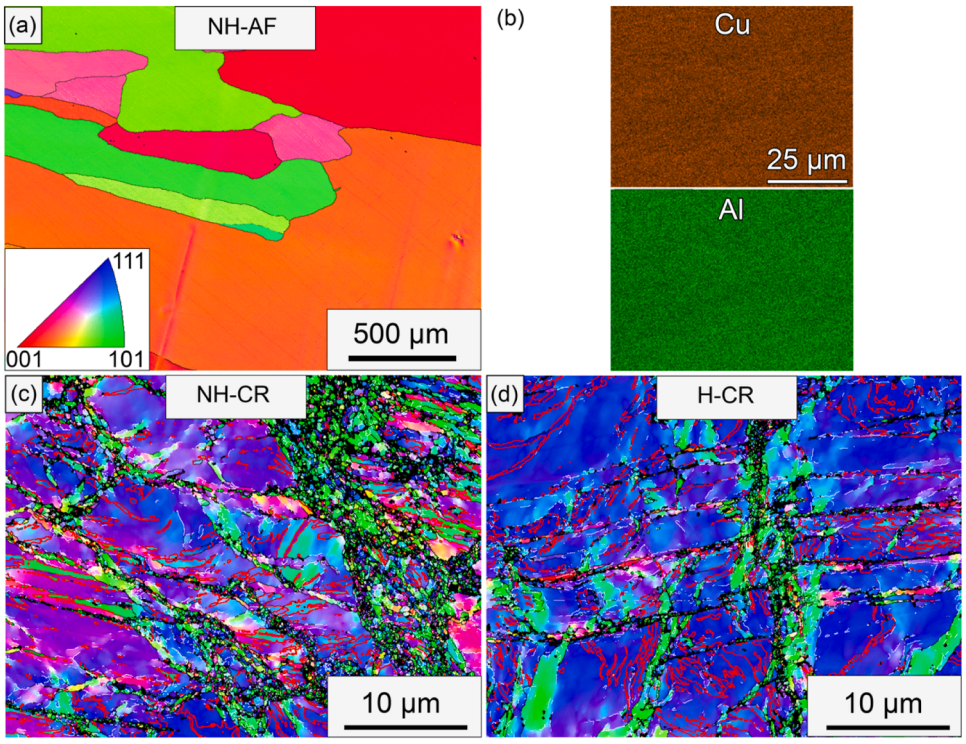


**Fig. 3.** (a) A typical EBSD IPF map and (b) the corresponding SEM-EDS maps of an NH-AF sample. (c) and (d) EBSD IPF maps of NH-CR and H-CR samples, respectively. TBs are shown as red lines.

obtained from an sample. The average grain size of the twinned areas is 1.14 ± 0.25 μm (including TBs). The grain size of the shear banding areas is 270 ± 120 nm.

Fig. 4a shows a low-magnification STEM BF image of an NH-CR sample, demonstrating the presence of nanograins. Fig. 4b presents a STEM-HAADF image with a higher magnification, captured from the red square region in Fig. 4a. Within one nanograin, localized contrast variation is observed, indicating the presence of compositional heterogeneities. Fig. 4c presents an atomic-resolution STEM-HAADF image taken along a ⟨110⟩ zone axis, showing localized contrast variation. Given that the atomic numbers of Al and Cu are 13 and 29, respectively, regions with bright contrast in the STEM-HAADF images are Cu-rich. In contrast, dark contrast regions are Al-rich, suggesting the existence of nano-scale compositional heterogeneity in the sample.

### 3.3. Microstructure and composition in recrystallized samples

Fig. 5a illustrates an EBSD IPF map of an NH-R sample. Fig. 5b presents the corresponding grain boundary (GB) map showing three types of GBs in the sample: low-angle GBs (LAGBs) with misorientation angles 2° – 10°, high-angle GBs (HAGBs) with misorientation angles >10°, and 60° associated with ⟨111⟩ TBs, which are delineated with white, black, and red lines, respectively. This sample exhibits a relatively high density of twins. These twins are mainly annealing twins as judged based on their relatively high thicknesses (> 2 mm), a typical characteristic of twins in fully recrystallized FCC metallic materials with low stacking fault energy (SFE) [13] (the SFE of the alloy is 13 mJ/m$^2$ [34]). Fig. 5c presents an EBSD IPF map taken from an H-R sample, and its corresponding GB map is displayed in Fig. 5d. There are no noticeable differences in grain size (27.3 ± 4.0 mm for NH-R and 24.0 ± 4.0 mm for H-R) and twin density (34 % for NH-R and 33 % for H-R) between these two types of samples. Both the fully recrystallized NH-R and H-R samples exhibit random textures. Comparisons have been made between samples under the same thermomechanical process. The microstructure remains the same.

The APT technique allows for quantitative detection of nanoscale compositional variations within the samples. Fig. 6a and b present APT data for Cu (orange) and Al (cyan) in NH-R and H-R samples,

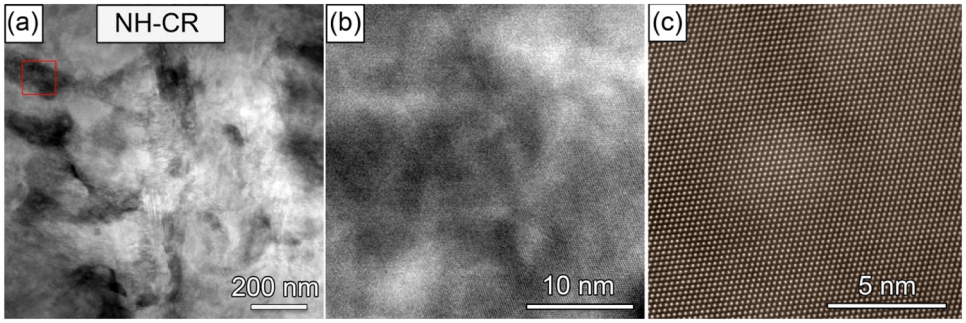


**Fig. 4.** STEM images taken from an NH-CR sample. (a) A low-magnification STEM-BF image showing the presence of nanograins. (b) A STEM-HAADF image taken from the red square area in (a), revealing localized contrast variation within a nano grain, which corresponds to compositional heterogeneity. (c) An atomic-resolution HAADF image showing nano-scale compositional heterogeneity.

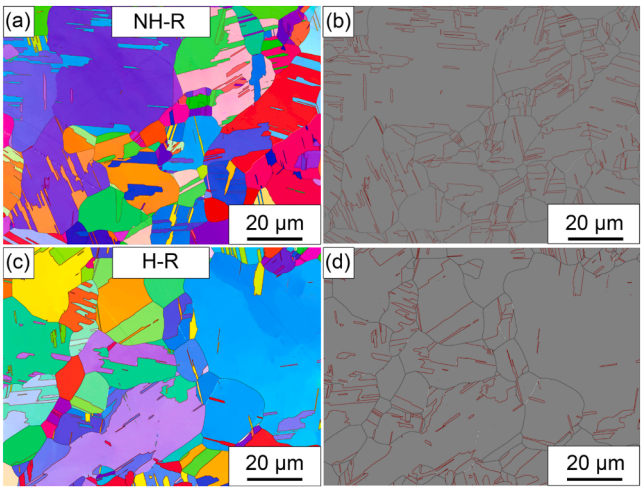


**Fig. 5.** (a) EBSD IPF map of an NH-R sample. (b) The corresponding GB map showing GB types. (c) EBSD IPF map of an H-R sample. (d) The corresponding GB map. White, black, and red lines in (b) and (d) represent LAGBs, HAGBs, and TBs, respectively.

respectively. Iso-concentration surfaces at 13 at.% Al (cyan) are used to delineate the individual elemental enrichment in Fig. 6a. The NH-R sample shows concentration fluctuations within a length scale of less than 5 nm, whereas no obvious compositional heterogeneity was observed in the H-R sample (Fig. 6b). Fig. 6c and d present the compositional profiles of Cu and Al in the NH-R and H-R samples from areas highlighted with red and blue rectangles in Fig. 6a and 6b, respectively. The composition of Cu ranges from ~ 84.6 at.% to ~ 92.6 at.%, showing an 8 at.% compositional variation. On the other hand, the composition of Cu in the H-R sample varies from ~88.8 at.% to ~ 92.2 at.%, with only 3.4 at.% compositional variation. The APT elemental line profiles of the NH-R sample reveal concentration fluctuations within nano-sized domains, with a length scale of less than 0.5 nm.

Fig. S1 presents a series of STEM images taken from an NH-R sample. Fig. S1a presents a selected area electron diffraction pattern (SAED) taken along a ⟨100⟩ zone axis, showing the expected FCC spots without extra reflections. This indicates no chemical short-range order. Fig. S1b–d present STEM-HAADF images taken with a camera length of 91 mm, 73 mm, and 58 mm, respectively. Contrast variation is observed in the NH-R sample, indicating local compositional heterogeneities. Fig. S1e presents an SAED pattern taken from a ⟨110⟩ zone axis. The corresponding STEM-HAADF images confirm the existence of local compositional heterogeneities, as evidenced by Fig. S1f–h.

Fig. 7a and b present atomic-resolution STEM-HAADF images taken from an NH-R sample and an H-R sample, respectively, along a ⟨110⟩ zone axis. Contrast variation is observed in the NH-R sample. The measured {111} interplanar distances in a bright-contrast and a dark-contrast area in Fig. 7a are 0.209 and 0.212 nm, which corresponds to the FCC lattice parameters of 0.362 and 0.367 nm, respectively. In contrast, the image from the H-R sample presents uniform contrast, indicating a homogenous distribution of Cu and Al elements. The measured {111} interplanar distance indicates an FCC lattice parameter of 0.363 nm.

Fig. 7c presents intensity profiles generated along the white arrows in Fig. 7a and b. The average intensity of the NH-R sample is higher than that of the H-R sample, indicating a higher average thickness of the NH-R TEM sample. The intensity variation in the STEM-HAADF image from the NH-R sample (0.8 KCounts) is ~4 times greater than that from the H-R sample (0.2 KCounts), clearly demonstrating compositional heterogeneity in the NH sample. This shows that the compositional heterogeneity was eliminated by the homogenization heat treatment.

To confirm the contrast differences in the STEM-HAADF images come from compositional heterogeneities, STEM-EDS was performed. Fig. 8a presents a STEM-HAADF image taken along a ⟨110⟩ zone axis from an NH-R sample. The corresponding EDS map of Cu and Al are given in Fig. 8b and c, respectively. The dark contrast area in the HAADF image is enriched in Al. Fig. 8d presents an EDS 1D concentration profile recorded across the white arrow in Fig. 8a. The average concentration of Al increased from 8 at.% in the bright contrast area to 10.5 at.% in the dark contrast area. Concentration fluctuations within nano-sized domains are also observed from the EDS analysis. The composition of Cu

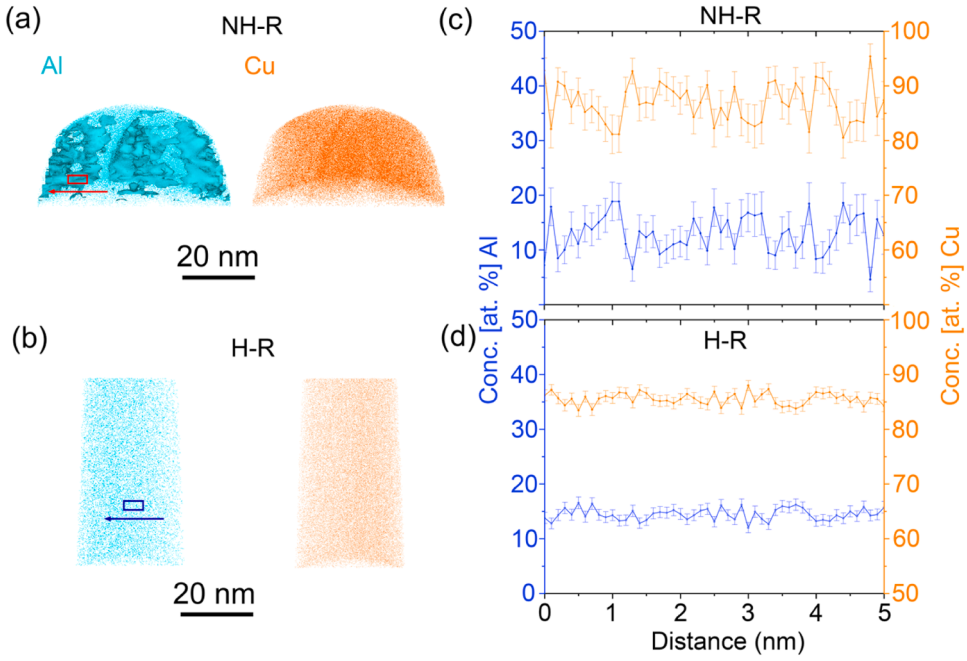


**Fig. 6.** (a) Atom distribution maps of Cu and Al from an NH-R sample. Filtered 13 at.% Al isoconcentration surfaces are highlighted using the cyan colour. (b) Atom distribution maps of Cu and Al from an H-R sample. (c) 1D concentration profile from the red Region of Interest in (a). (d) 1D concentration profile from the blue Region of Interest in (b).

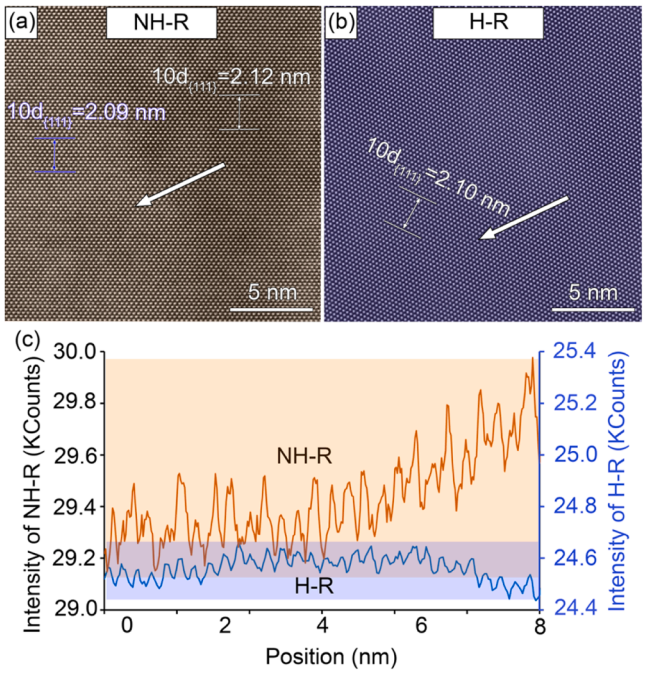


**Fig. 7.** (a) Atomic-resolution STEM-HAADF images taken from (a) an NH-R sample and (b) an H-R sample. (c) The intensity profiles generated along the white arrows in (a) and (b), with the intensity variation ranges indicated by orange and blue rectangles, respectively.

ranges from ~ 87.9 at.% to ~ 92.9 at.%, showing 4 at.% compositional variation. The variation is only half the value of that from the APT result because EDS results are the average concentration generated from the local region along the electron beam direction. To confirm the contrast and compositional variations in Fig. 8a were not caused by local specimen thickness variation, EELS thickness mapping was conducted and the corresponding thickness profile is presented in Fig. 8e and f, indicating relatively uniform local specimen thickness of ~ 53 nm. Therefore, the local concentration is the averaged value of the volumn along the electron beam direction, which results in a lower concentration variation than those presented in the APT data in Fig. 6. The concentration fluctuations within nano-sized domains have been revealed in Fig. 6c. The length scale of the concentration fluctuations is less than 0.5 nm, which is consistent with the APT results.

To further visualize the degree of compositional heterogeneity, the STEM imaging technique was used to map the local electric field, which provides information on the local charge distribution and bonding strength [35]. Compositional heterogeneity leads to local deviations from the nominal composition, resulting in the variation of bonding strength. The resulting local electric field maps of areas in the NH-R and H-R samples are presented in Fig. 9a and b, respectively. The direction and amplitude of local electric fields are presented in different colours, as shown by the colour wheel in the upper-right corner. The local electric field in the NH-R sample exhibits irregularly shaped local domains with varying directions and amplitudes, in contrast to the relatively uniform map generated from the H-R sample. The average size of these domains is below 5 nm, consistent with the sizes of compositional heterogeneities observed in STEM-HAADF images.

To ensure compositional heterogeneity is the dominant factor contributing to the mechanical property differences instead of other structural factors, e.g. grain size, texture, GB segregation, and dislocation density, in-situ compression tests of single crystalline micropillars were performed. The single crystalline micropillar samples were compressed along a ⟨001⟩ direction. Fig. 10a and b present SEM secondary electron images taken from deformed NH-R and H-R pillars, respectively. {111} slip traces, marked by red dashed lines, can be observed on the surfaces of both pillars. A white arrow points to a catastrophic collapse of the NH-R pillar. The corresponding engineering stress–strain curves are given in Fig. 10c. The average YS is around 280 MPa for NH-R samples in contrast to 215 MPa for H-R samples. The average engineering stress value at 30 % engineering strain is around 520 MPa for NH-R samples in contrast to 475 MPa for H-R samples. Moreover, the

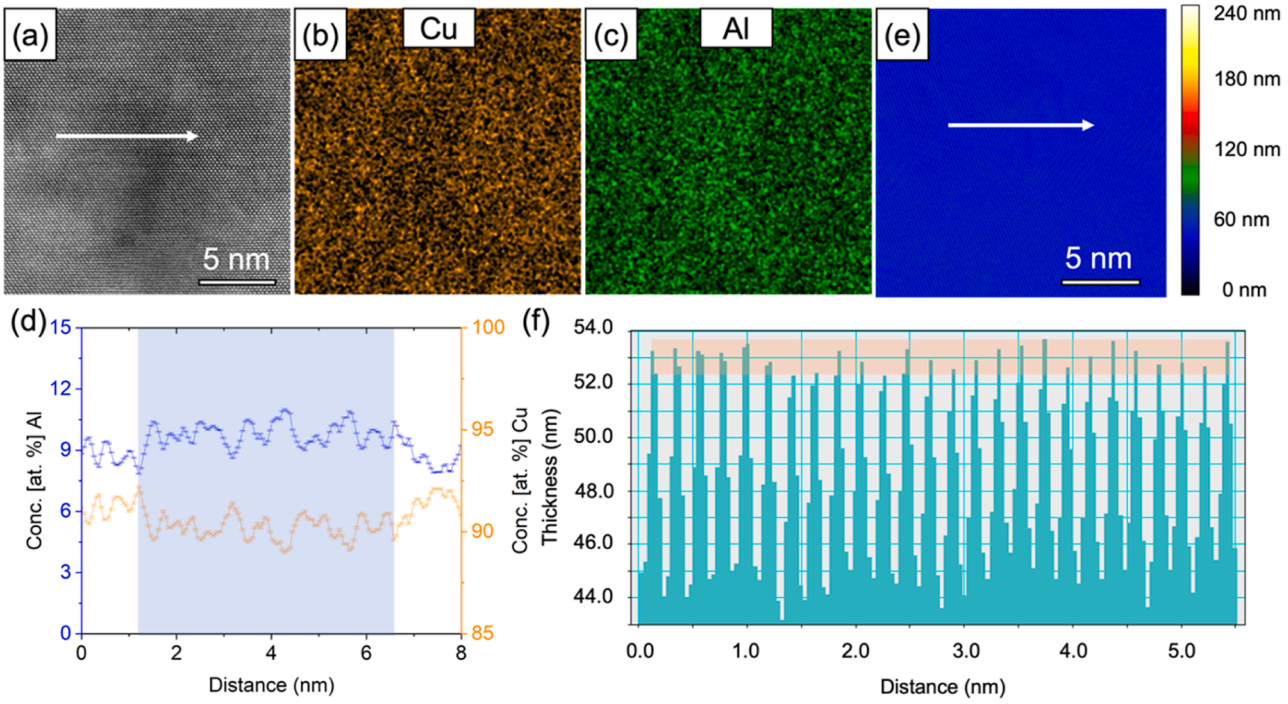


**Fig. 8.** (a) A STEM-HAADF image taken along a ⟨110⟩ zone axis from an NH-R sample. (b -c) The corresponding EDS maps of Cu and Al, respectively. (d) 1D concentration profile recorded across the white arrow in a. The shaded blue rectangle indicates the area enriched in Al. (e) An EELS thickness map taken from the same region as (a). (f) A thickness profile recorded across the white arrow in e.

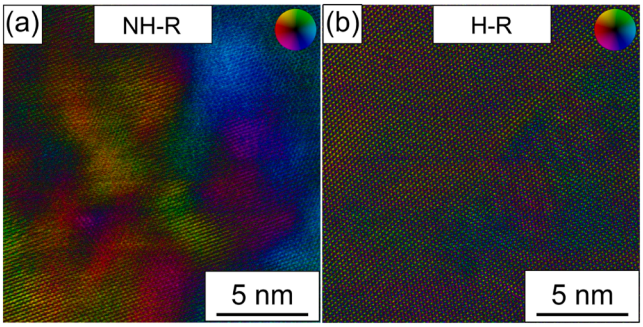


**Fig. 9.** (a) and (b) Typical differential phase contrast maps taken from NH-R and H-R samples, respectively, showing variations in the direction and amplitude of the local electric field introduced by local compositional heterogeneities. The resulting colors on the maps are represented by the colour wheel in the upper-right corner.

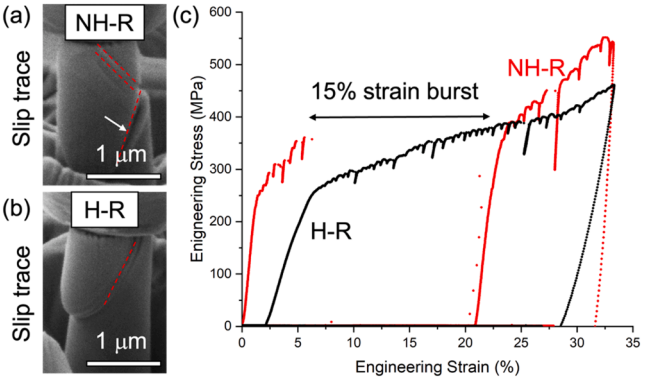


**Fig. 10.** SEM images taken from a deformed NH-R pillar (a) and a deformed H-R pillar (b). Red dashed lines mark {111} slip traces. The white arrow in (a) points to a catastrophic collapse of the NH-R pillar. (c) Engineering stress–strain curves taken from typical NH-R and H-R pillars.

NH-R sample (red curve) exhibited a more intermittent deformation process and more catastrophic strain bursts than the H-R one (black curve). The largest burst found in the NH-R sample resulted in a sudden strain increment of more than 15 %, whereas no burst in the homogeneous sample exceeded 5 %. The occurrence of strain bursts is a common feature of mechanical testing of submicron- or nano-scale single crystals due to the limited number of slip systems and scarce dislocation sources [36–39]. Small- and intermediate-size strain bursts are featured as frequent fluctuations on stress–strain curves and would lead to temporal detaches of the pillar from the indenter. These bursts are believed to result from the collective motion of a relatively small number of dislocations and normally result in slip of short distances on the surface of pillars [40–42]. Whereas large strain bursts that would lead to a catastrophic collapse of pillars, like the one indicated by the white arrow in Fig. 10a, usually arise from a more explosive manner of dislocation motion, involving the abrupt activation of a large number of dislocations from multiple sources simultaneously [42,43]. In the NH-R sample, the occurrence of extremely large strain bursts was likely caused by the compositional heterogeneity distributed in the sample, which were able to act as effective dislocation pinning sites. These obstacles led to the accumulation of dislocations, contributing to the hardening of the sample. As the flow stress increased, the pinning sites were overcome, giving rise to the sudden release of massive dislocations and causing a large burst in the stress–strain curve.

### 3.4. Fracture surface analyses

SEM SE2 images were taken from the fracture surfaces of the NH-R and H-R samples, which are presented in Fig. 11a and b, respectively. The fracture surface of the NH-R sample presents both fine dimples and quasi-cleavage fracture surfaces, as pointed out by black and white arrows, respectively. On the contrary, the fracture surface of the H-R sample is dominated by fine dimples with similar average sizes (3 μm) as those in the NH-R sample, indicating better ductility. The underlying mechanism of the loss of ductility will be discussed in the next section.

### 3.5. Strain hardening due to back stress

To probe the mechanism of transient hardening, LUR tests (Fig. 12a) were conducted on NH-R and H-R samples. The YS of the NH-R is 20 MPa higher than that of the H-R sample, indicating the strengthening effect of compositional heterogeneities on YS. Meanwhile, hysteresis loops are observed in the NH-R sample (Fig. 12b), indicating the presence of the Bauschinger effect [44]. The contributions of the back stress and dislocation hardening to the flow stress can be estimated [45–47]. The back stress can be calculated as $\sigma_b = \sigma_0 - \sigma_{eff}$ and $\sigma_{eff} = (\sigma_0 - \sigma_u)/2 + (\sigma^*/2)$ [45], where $\sigma_b$ denotes the back stress, $\sigma_{eff}$ is the effective stress, $\sigma_0$ is the flow stress, $\sigma_u$ is the unloading yield stress, and $\sigma^*$ is the viscous stress. These parameters are defined in Fig. 12b. $\sigma_b$ is associated with a long-range stress on mobile dislocations and $\sigma_{eff}$ is the stress required for a dislocation to overcome local obstacles. As shown in Fig. 12c, the back stress increases from about 173 MPa to 290 MPa with increasing strain, which contributes to the high strain hardening in an NH-R sample. This is the primary reason why the strain hardening in the NH-R sample increased with applied plastic strain and surpassed that of the H-R sample, as shown in Fig. 2b. The effective stress, which includes the dislocation hardening, is much lower than the back stress. The increase in the effective stress with tensile strain should be caused by dislocation hardening [47]. Therefore, the high strain hardening originates from both back stress hardening and dislocation hardening.

## 4. Discussion

The experimental results presented above reveal that the WAAM process of Cu-9Al leads to the formation of nano-scale compositional heterogeneity, as shown by STEM-HAADF and APT analyses. This heterogeneity can be effectively eliminated through a long-time homogenization heat treatment. The impact of compositional heterogeneity on mechanical properties has also been evaluated. In samples with ultrafine-grained microstructures, both the YS and UTS show improvements of $> 4\%$ in samples with compositional heterogeneity, albeit with a slight reduction in ductility ($< 3\%$). However, in CG samples, the YS increment is negligible, while a significant loss of ductility (16 %) is observed. For CG materials, the homogenization process plays a crucial role in improving mechanical properties. In this section, we aim to provide a rationalization for and discussion of the aforementioned observations.

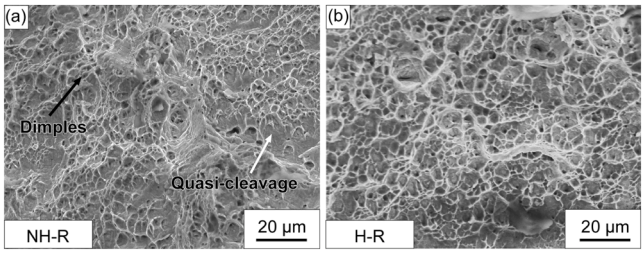


**Fig. 11.** (a) The fracture surface of the NH-R sample. The white and black arrows indicate the quasi-cleavage fracture surface and fine dimples, respectively. (b) The fracture surface of the H-R sample.

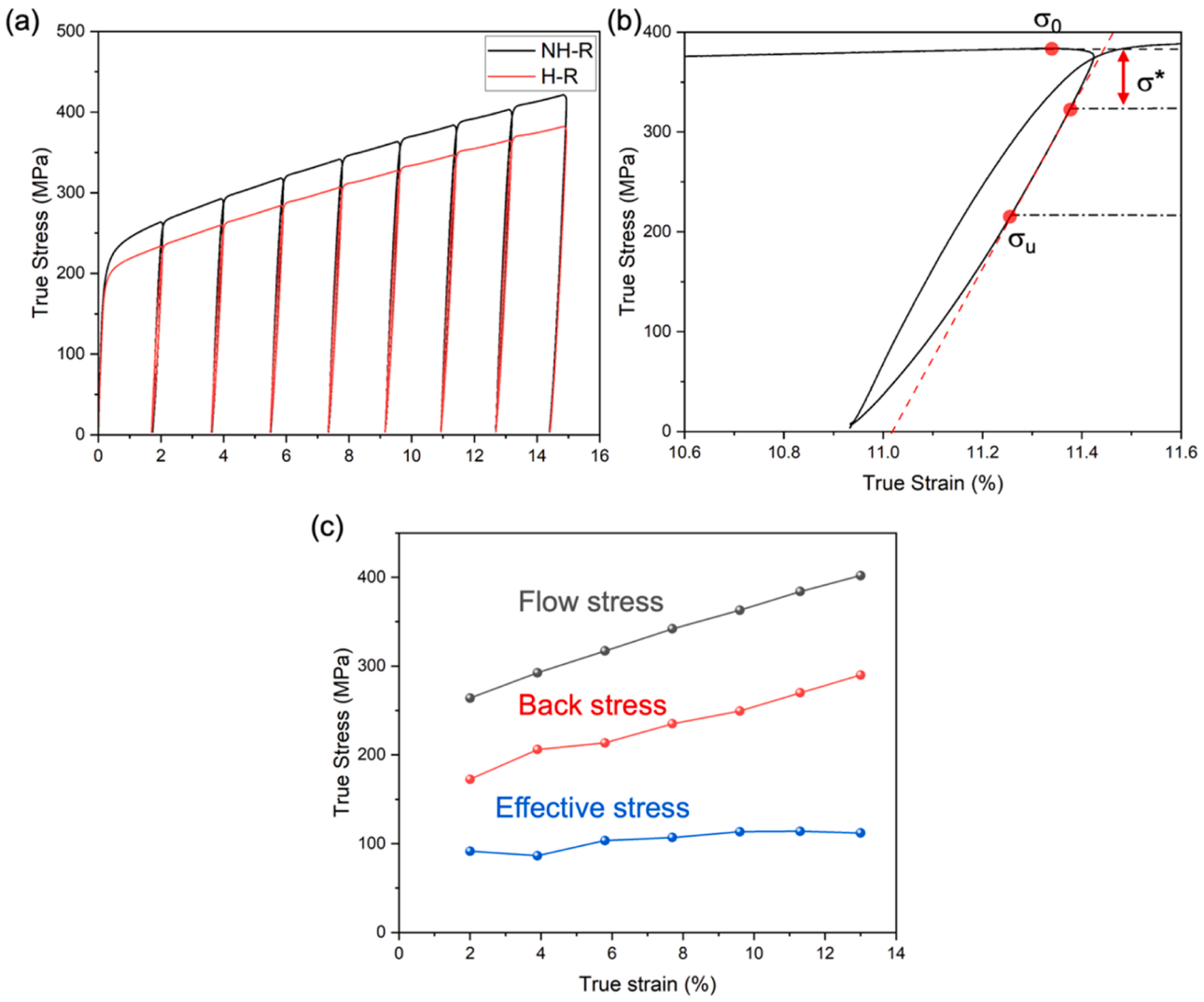


**Fig. 12.** (a) LUR true stress–strain curve taken from NH-R and H-R samples. (b) A representative LUR cycle showing the hysteresis loop from an NH-R sample. $\sigma_0$ denotes the flow stress before unloading, $\sigma_u$ the unloading yield stress, and $\sigma^*$ the viscous stress. (c) Flow stress, back stress, and effective stress versus true strain in an NH-R sample.

Previous research demonstrated that introducing compositional heterogeneity can improve the YS, work hardening behaviour, and even the ductility of CrCoNi medium-entropy alloys [48]. Li et al. [3] reported that compositional undulation with compositional domain sizes of $<$ 10 nm in nanocrystalline Ni-Co alloys significantly slows down dislocation slip, and promotes dislocation interaction and accumulation in the severely limited space inside nanocrystalline grains [3]. These effectively increase the flow stress and promote the dislocation storage capacity and therefore, the ductility [3]. In alloys with high solute concentration, e.g., high-entropy alloys, the solute–dislocation interactions always provide an extra energy barrier to dislocation slip [6]. The work hardening rate in Cu-Al alloys increases with increasing Al content [49]. A transient hardening behaviour has been observed in NH-R samples in the current study. Similar work hardening behaviour was previously reported in gradient-structured materials [50] and high-Mn steels [51]. The reported transient hardening has been attributed to either the grain-size gradient structure or the presence of hard, nano-sized carbides. However, these two conditions do not apply to our samples because the Cu-Al system with Al concentrations $<$ 16 at.% is free from potential complications and possesses no secondary phase. In general, the concentration undulation is within the range of $\pm$ 5 at.% around the global or nominal composition. Each grain contains regions with varying compositions, with compositional domains consisting of "soft" (low Al concentration) and "hard" regions (high Al concentration) within individual CGs. The local Al concentration varies from 7.4 at.% to 15.4 at.%, which has been shown to result in a 20 % enhancement of both YS and UTS in a CG Cu-Al alloy [52]. An elastic–plastic deformation stage is reached where soft domains undergo plastic deformation under uniaxial tension, while hard domains remain elastic [53]. When the hard domains start to deform plastically, dislocation interactions in these domains provide extra work hardening, resulting in the observed transient hardening behaviour and strong back-stress hardening [46,47,54,55]. Meanwhile, the extra work hardening in our sample is hypothesized to be caused by the strain gradient due to the different mechanical behaviours of the hard and soft domains under uniaxial tension [50]. Previous studies have reported that this extra work hardening is accommodated by dislocations [50,56,57]. Dislocations interact and tangle with each other, as evidenced by our in-situ micropillar compression tests, effectively promoting dislocation storage near the boundaries between the hard and soft regions, contributing to the observed additional hardening. Compared with other materials with a transient hardening behaviour, the work hardening rate at the transient point of our NH-R sample is higher with a value of $\sim$ 5 GPa. Grain size plays a key role here. With a small grain size, the work hardening rate decreases rapidly with increasing strain in the initial deformation stage [47,50]. For our CG samples (24 μm grain size), the work hardening rate

is overall higher than those with smaller grain sizes, e.g. ultra-fine grained, and drops more steadily. When the transient hardening occurred with a true strain value of 1 %, the corresponding work hardening rate still remained at a high value.

Compositional heterogeneities also affect the SFE of the Cu-Al alloy system. The SFE would vary by as much as 60 %, i.e., from ~ 20 $mJ/m^2$ when the Al concentration is 8 at.% to ~ 8 $mJ/m^2$ when the Al concentration is 15 at.% [58–60]. It is well recognised that reducing SFE promotes dislocation dissociation and deformation twinning but inhibits cross-slip, all of which can significantly enhance the work-hardening capabilities of materials and improve their mechanical properties [61].

However, in our CG binary Cu-Al system with a grain size of ~ 24 μm, the homogenized samples present better mechanical properties when compared to the NH samples. At an engineering strain level under 50 %, the strength of NH-R is higher than that of H-R samples, owing to the higher work hardening rate. However, the uniform elongation of the NH-R sample is 16 % lower than the H-R sample, resulting in a shorter plastic deformation stage. Consequently, the UTS of NH-R (430 MPa) is comparable to that of H-R samples (417 MPa). The NH samples display compositional undulations with a wavelength of ~ 5 nm, which falls within the range observed in nanocrystalline Ni-Co alloys for simultaneous improvement of strength and ductility [3]. Grain size plays a key role in retaining uniform elongation. For nanocrystalline materials, the low work hardening rate and low dislocation accumulation limit the ductility of the materials [62]. In those cases, the grain sizes are so small that dislocation sources no longer exist in the grain interior, and GBs become dislocation sources and sink without much dislocation accumulation within grains [63,64]. Therefore, a small increase in dislocation storage capacity becomes significant for improving the strain hardening rate and, consequently, ductility. In contrast, there is enough room for dislocation accumulation within the grains in CG materials. Impeding dislocation motion by compositional heterogeneity does not significantly contribute to improving the dislocation storage capability. However, the negative effect of compositional heterogeneity leads to quasi-cleavage that reduces ductility due to the early failure of hard regions [50]. The quasi-cleavage fracture is also observed in our NH-AF samples. Although this type of fracture surface can be observed in ductile materials, the 16 % ductility loss indicates that compositional heterogeneity reduces the ductility of materials with coarser grain sizes [25]. In this study, tensile tests at a quasi-static strain rate were conducted to study the effect of compositional heterogeneity on mechanical properties. Increasing strain rate would lead to higher flow stresses because of the increased barriers to dislocation motion [55]. Further studies need to be conducted on the strain rate sensitivity of the strengthening effect of compositional heterogeneity.

## 5. Conclusions

In summary, we have investigated the impact of compositional heterogeneity on the mechanical behaviour of Cu-9Al binary alloy samples with varying grain sizes. The alloy was manufactured using the WAAM technique, followed by various types of subsequent treatments to achieve various microstructures. APT, EDS, and STEM-HAADF imaging revealed compositional heterogeneity in the size of ~ 5 nm that can be removed by a long-time homogenization heat treatment. In samples with relatively small grain size (~ 300 nm), the compositional undulation, which affects local SFE, imposes resistance to dislocation slip and promotes dislocation accumulation, resulting in further strain hardening. However, in coarse-grained (~24 μm) samples, the presence of hard regions results in reduced ductility and early fracture. Therefore, overall improvement of strength and ductility by compositional heterogeneity is only applicable to smaller grain sizes, e.g. ultra-fine-grained and nanocrystalline samples.

## Declaration of Competing Interest

The authors declare that they have no known competing financial interests or personal relationships that could have appeared to influence the work reported in this paper.

## Acknowledgements

This project is supported by the Australia–US Multidisciplinary University Research Initiative (AUSMURI) program (3Dadditive.com.au). XZL, ZXP, NH, SP, and SPR were also supported by the Australian Research Council [DP190102243, DP230100183, DP230101063, and DP200100940]. ZBC would like to express his sincere thanks for the financial support from the Research Office of The Hong Kong Polytechnic University (Project codes: P0041361 and P0039966). The authors acknowledge the scientific and technical input and support from Sydney Microscopy & Microanalysis—a core research facility of the University of Sydney and the University's node of Microscopy Australia.

## Supplementary materials

Supplementary material associated with this article can be found, in the online version, at doi:10.1016/j.actamat.2023.119531.

## References

[1] S.P. Ringer, K. Hono, T. Saksai, I.J. Polmear, Cluster hardening in an aged Al-Cu-Mg alloy, Scr Mater. 36 (1997) 517–538, https://doi.org/10.1016/S1359-6462(96)00415-0.
[2] S.P. Ringer, T. Sakurap, I.J. Polmear, Origins of hardening in aged Al-Cu-Mg-(Ag) alloys, Acta Matrr. 45 (1997) 3731–3744, https://doi.org/10.1016/S1359-6454(97)00039-6.
[3] H. Li, H. Zong, S. Li, S. Jin, Y. Chen, M.J. Cabral, B. Chen, Q. Huang, Y. Chen, Y. Ren, K. Yu, S. Han, X. Ding, G. Sha, J. Lian, X. Liao, E. Ma, J. Sun, Uniting tensile ductility with ultrahigh strength via composition undulation, Nature 604 (2022) 273–279, https://doi.org/10.1038/s41586-022-04459-w.
[4] Y. Bu, Y. Wu, Z. Lei, X. Yuan, H. Wu, X. Feng, J. Liu, J. Ding, Y. Lu, H. Wang, Z. Lu, W. Yang, Local chemical fluctuation mediated ductility in body-centered-cubic high-entropy alloys, Mater. Today 46 (2021) 28–34, https://doi.org/10.1016/j.mattod.2021.02.022.
[5] E. Ma, X. Wu, Tailoring heterogeneities in high-entropy alloys to promote strength–ductility synergy, Nat. Commun. 10 (2019) 1–10, https://doi.org/10.1038/s41467-019-13311-1.
[6] M. Shih, J. Miao, M. Mills, M. Ghazisaeidi, Stacking fault energy in concentrated alloys, Nat. Commun. 12 (2021) 1–10, https://doi.org/10.1038/s41467-021-23860-z.
[7] Z. Dong, W. Li, S. Schönecker, B. Jiang, L. Vitos, Invariant plastic deformation mechanism in paramagnetic nickel-iron alloys, Proc. Natl. Acad. Sci. USA. 118 (2021) 1–5, https://doi.org/10.1073/pnas.2023181118.
[8] Q. Ding, Y. Zhang, X. Chen, X. Fu, D. Chen, S. Chen, L. Gu, F. Wei, H. Bei, Y. Gao, M. Wen, J. Li, Z. Zhang, T. Zhu, R.O. Ritchie, Q. Yu, Tuning element distribution, structure and properties by composition in high-entropy alloys, Nature 574 (2019) 223–227, https://doi.org/10.1038/s41586-019-1617-1.
[9] Q.J. Li, H. Sheng, E. Ma, Strengthening in multi-principal element alloys with local-chemical-order roughened dislocation pathways, Nat. Commun. 10 (2019) 1–11, https://doi.org/10.1038/s41467-019-11464-7.
[10] Y. Chen, Y. Fang, X. Fu, Y. Lu, S. Chen, H. Bei, Q. Yu, Origin of strong solid solution strengthening in the CrCoNi-W medium entropy alloy, J. Mater. Sci. Technol. 73 (2021) 101–107, https://doi.org/10.1016/j.jmst.2020.08.058.
[11] J. Ding, Q. Yu, M. Asta, R.O. Ritchie, Tunable stacking fault energies by tailoring local chemical order in CrCoNi medium-entropy alloys, Proc. Natl. Acad. Sci. USA. 115 (2018) 8919–8924, https://doi.org/10.1073/pnas.1808660115.
[12] M.N. Hasan, J. Gu, S. Jiang, H.J. Wang, M. Cabral, S. Ni, X.H. An, M. Song, L. M. Shen, X.Z. Liao, Effects of elemental segregation on microstructural evolution and local mechanical properties in a dynamically deformed CrMnFeCoNi high entropy alloy, Scr. Mater. 190 (2021) 80–85, https://doi.org/10.1016/j.scriptamat.2020.08.048.
[13] H. Wang, D. Chen, X. An, Y. Zhang, S. Sun, Y. Tian, Z. Zhang, A. Wang, J. Liu, M. Song, S.P. Ringer, T. Zhu, X. Liao, Deformation-induced crystalline-to-amorphous phase transformation in a CrMnFeCoNi high-entropy alloy, Sci Adv. 7 (2021), https://doi.org/10.1126/sciadv.abe3105.
[14] S. Gorsse, C. Hutchinson, M. Gouné, R. Banerjee, Additive manufacturing of metals: a brief review of the characteristic microstructures and properties of steels, Ti-6Al-4 V and high-entropy alloys, Sci. Technol. Adv. Mater. 18 (2017) 584–610, https://doi.org/10.1080/14686996.2017.1361305.
[15] L.E. Murr, S.M. Gaytan, D.A. Ramirez, E. Martinez, J. Hernandez, K.N. Amato, P. W. Shindo, F.R. Medina, R.B. Wicker, Metal fabrication by additive manufacturing

using laser and electron beam melting technologies, J. Mater. Sci. Technol. 28 (2012) 1–14, https://doi.org/10.1016/S1005-0302(12)60016-4.
[16] T. Song, Z. Chen, X. Cui, S. Lu, H. Chen, H. Wang, T. Dong, B. Qin, K.C. Chan, M. Brandt, X. Liao, S.P. Ringer, M. Qian, Strong and ductile titanium–oxygen–iron alloys by additive manufacturing, Nature 618 (2023) 63–68, https://doi.org/10.1038/s41586-023-05952-6.
[17] B. Wu, Z. Pan, D. Ding, D. Cuiuri, H. Li, J. Xu, J. Norrish, A review of the wire arc additive manufacturing of metals: properties, defects and quality improvement, J. Manuf. Process. 35 (2018) 127–139, https://doi.org/10.1016/j.jmapro.2018.08.001.
[18] Y.M. Wang, T. Voisin, J.T. McKeown, J. Ye, N.P. Calta, Z. Li, Z. Zeng, Y. Zhang, W. Chen, T.T. Roehling, R.T. Ott, M.K. Santala, P.J. Depond, M.J. Matthews, A. V. Hamza, T. Zhu, Additively manufactured hierarchical stainless steels with high strength and ductility, Nat. Mater. 17 (2018) 63–70, https://doi.org/10.1038/NMAT5021.
[19] Y. Kok, X.P. Tan, P. Wang, M.L.S. Nai, N.H. Loh, E. Liu, S.B. Tor, Anisotropy and heterogeneity of microstructure and mechanical properties in metal additive manufacturing : a critical review, Mater. Des. 139 (2018) 565–586, https://doi.org/10.1016/j.matdes.2017.11.021.
[20] D. Herzog, V. Seyda, E. Wycisk, C. Emmelmann, Additive manufacturing of metals, Acta Mater. 117 (2016) 371–392, https://doi.org/10.1016/j.actamat.2016.07.019.
[21] D. Zhang, D. Qiu, M.A. Gibson, Y. Zheng, H.L. Fraser, D.H. Stjohn, M.A. Easton, Additive manufacturing of ultrafine-grained high-strength titanium alloys, Nature (2019) 576, https://doi.org/10.1038/s41586-019-1783-1.
[22] H. Wang, Z.G. Zhu, H. Chen, A.G. Wang, J.Q. Liu, H.W. Liu, R.K. Zheng, S.M.L. Nai, S. Primig, S.S. Babu, S.P. Ringer, X.Z. Liao, Effect of cyclic rapid thermal loadings on the microstructural evolution of a CrMnFeCoNi high-entropy alloy manufactured by selective laser melting, Acta Mater. 196 (2020) 609–625, https://doi.org/10.1016/j.actamat.2020.07.006.
[23] W. Xu, M. Brandt, S. Sun, J. Elambasseril, Q. Liu, K. Latham, K. Xia, M. Qian, Additive manufacturing of strong and ductile Ti-6Al-4 V by selective laser melting via in situ martensite decomposition, Acta Mater. 85 (2015) 74–84, https://doi.org/10.1016/j.actamat.2014.11.028.
[24] S. Zhu, H.C. Shih, X. Cui, C.Y. Yu, S.P. Ringer, Design of solute clustering during thermomechanical processing of AA6016 Al–Mg–Si alloy, Acta Mater. 203 (2021), https://doi.org/10.1016/j.actamat.2020.10.074.
[25] B. Dong, Z. Pan, C. Shen, Y. Ma, H. Li, Fabrication of Copper-Rich Cu-Al Alloy Using the Wire-Arc Additive Manufacturing Process, Metall. Mater. Trans. B 48 (2017) 3143–3151, https://doi.org/10.1007/s11663-017-1071-0.
[26] M.K. Miller, A. Cerezo, M.G. Hetherington, G.D.W. Smith FRS, Atom Probe Field Ion Microscopy, Calrendon Press, Oxford, UK, 1996.
[27] P.W. Trimby, Y. Cao, Z. Chen, S. Han, K.J. Hemker, J. Lian, X. Liao, P. Rottmann, S. Samudrala, J. Sun, J.T. Wang, J. Wheeler, J.M. Cairney, Characterizing deformed ultrafine-grained and nanocrystalline materials using transmission Kikuchi diffraction in a scanning electron microscope, Acta Mater. 62 (2014) 69–80, https://doi.org/10.1016/j.actamat.2013.09.026.
[28] T. Malis, S.C. Cheng, R.F. Egerton, EELS log-ratio technique for specimen-thickness measurement in the TEM, J. Electron Microsc. Tech. 8 (1988) 193–200, https://doi.org/10.1002/jemt.1060080206.
[29] K. Iakoubovskii, K. Mitsuishi, Y. Nakayama, K. Furuya, Thickness measurements with electron energy loss spectroscopy, Microsc. Res. Tech. 71 (2008) 626–631, https://doi.org/10.1002/jemt.20597.
[30] S.J. Pennycook, Z-contrast stem for materials science, Ultramicroscopy 58 (1989) 58–69.
[31] I. Lazić, E.G.T. Bosch, S. Lazar, Phase contrast STEM for thin samples: integrated differential phase contrast, Ultramicroscopy 160 (2016) 265–280, https://doi.org/10.1016/j.ultramic.2015.10.011.
[32] M.D. Uchic, D.M. Dimiduk, J.N. Florando, W.D. Nix, Sample dimensions influence strength and crystal plasticity, Science (1979) 305 (2004) 986–989, https://doi.org/10.1126/science.1098993.
[33] J.J. Friel, C.E. Lyman, Tutorial review: x-ray mapping in electron-beam instruments, Microsc. Microanal. 12 (2006) 2–25, https://doi.org/10.1017/S1431927606060211.
[34] T.C. Schulthess, P.E.A. Turchi, A. Gonis, T.-G. Nieh, Systematic study of stacking fault energies of random Al-based alloys, Acta Mater. 46 (1998), 22152221, https://doi.org/10.1016/S1359-6454(97)00432-1.
[35] N. Shibata, T. Seki, G. Sánchez-Santolino, S.D. Findlay, Y. Kohno, T. Matsumoto, R. Ishikawa, Y. Ikuhara, Electric field imaging of single atoms, Nat. Commun. 8 (2017), https://doi.org/10.1038/ncomms15631.
[36] J.Y. Kim, D. Jang, J.R. Greer, Tensile and compressive behavior of tungsten, molybdenum, tantalum and niobium at the nanoscale, Acta Mater. 58 (2010) 2355–2363, https://doi.org/10.1016/j.actamat.2009.12.022.
[37] S. Lee, A. Vaid, J. Im, B. Kim, A. Prakash, J. Guénolé, D. Kiener, E. Bitzek, S.H. Oh, In-situ observation of the initiation of plasticity by nucleation of prismatic dislocation loops, Nat. Commun. 11 (2020), https://doi.org/10.1038/s41467-020-15775-y.
[38] R. Niu, X. An, L. Li, Z. Zhang, Y.W. Mai, X. Liao, Mechanical properties and deformation behaviours of submicron-sized Cu–Al single crystals, Acta Mater. 223 (2022), https://doi.org/10.1016/j.actamat.2021.117460.
[39] K.Y. Xie, S. Shrestha, Y. Cao, P.J. Felfer, Y. Wang, X. Liao, J.M. Cairney, S. P. Ringer, The effect of pre-existing defects on the strength and deformation behavior of α-Fe nanopillars, Acta Mater. 61 (2013) 439–452, https://doi.org/10.1016/j.actamat.2012.09.022.
[40] F.F., M.C., W.D., Z.M. & Z.S. Csikor, Dislocation avalanches, strain bursts, and the problem of plastic forming at the micrometer scale, Science (1979) 318 (2007) 251–254, https://doi.org/10.1126/science.1143719.
[41] Z.J. Wang, Q.J. Li, Z.W. Shan, J. Li, J. Sun, E. Ma, Sample size effects on the large strain bursts in submicron aluminum pillars, Appl. Phys. Lett. 100 (2012), https://doi.org/10.1063/1.3681582.
[42] K.Y. Xie, S. Shrestha, Y. Cao, P.J. Felfer, Y. Wang, X. Liao, J.M. Cairney, S. P. Ringer, The effect of pre-existing defects on the strength and deformation behavior of α-Fe nanopillars, Acta Mater. 61 (2013) 439–452, https://doi.org/10.1016/j.actamat.2012.09.022.
[43] C.R. & C.W. Weinberger, Surface-controlled dislocation multiplication in metal micropillars, Proc. Natl. Acad. Sci. USA. 105 (2008) 14304–14307, https://doi.org/10.1073/pnas.0806118105.
[44] X. Feaugas, On the origin of the tensile flow stress in the stainless steel AISI 316 L at 300 K: back stress and effective stress, Acta Mater. 47 (1999) 3617–3632, https://doi.org/10.1016/S1359-6454(99)00222-0.
[45] Y. Xiang, J.J. Vlassak, Bauschinger effect in thin metal films, Scr. Mater. 53 (2005) 177–182, https://doi.org/10.1016/j.scriptamat.2005.03.048.
[46] M. Yang, Y. Pan, F. Yuan, Y. Zhu, X. Wu, Back stress strengthening and strain hardening in gradient structure, Mater. Res. Lett. 4 (2016) 145–151, https://doi.org/10.1080/21663831.2016.1153004.
[47] X. Wu, M. Yang, F. Yuan, G. Wu, Y. Wei, X. Huang, Y. Zhu, Heterogeneous lamella structure unites ultrafine-grain strength with coarse-grain ductility, Proc. Natl. Acad. Sci. USA. 112 (2015) 14501–14505, https://doi.org/10.1073/pnas.1517193112.
[48] R. Zhang, S. Zhao, J. Ding, Y. Chong, T. Jia, C. Ophus, M. Asta, R.O. Ritchie, A. M. Minor, Short-range order and its impact on the CrCoNi medium-entropy alloy, Nature 581 (2020) 283–287, https://doi.org/10.1038/s41586-020-2275-z.
[49] Y.Z. Tian, L.J. Zhao, N. Park, R. Liu, P. Zhang, Z.J. Zhang, A. Shibata, Z.F. Zhang, N. Tsuji, Revealing the deformation mechanisms of Cu–Al alloys with high strength and good ductility, Acta Mater. 110 (2016) 61–72, https://doi.org/10.1016/j.actamat.2016.03.015.
[50] X. Wu, P. Jiang, L. Chen, F. Yuan, Y.T. Zhu, Extraordinary strain hardening by gradient structure, Proc. Natl. Acad. Sci. USA. 111 (2014) 7197–7201, https://doi.org/10.1073/pnas.1324069111.
[51] I. Gutierrez-Urrutia, D. Raabe, Influence of Al content and precipitation state on the mechanical behavior of austenitic high-Mn low-density steels, Scr. Mater. 68 (2013) 343–347, https://doi.org/10.1016/j.scriptamat.2012.08.038.
[52] S. Qu, X.H. An, H.J. Yang, C.X. Huang, G. Yang, Q.S. Zang, Z.G. Wang, S.D. Wu, Z. F. Zhang, Microstructural evolution and mechanical properties of Cu-Al alloys subjected to equal channel angular pressing, Acta Mater. 57 (2009) 1586–1601, https://doi.org/10.1016/j.actamat.2008.12.002.
[53] Y. Zhu, X. Wu, Heterostructured materials, Prog. Mater Sci. 131 (2023), https://doi.org/10.1016/j.pmatsci.2022.101019.
[54] M.X. Yang, F.P. Yuan, Q.G. Xie, Y.D. Wang, E. Ma, X.L. Wu, Strain hardening in Fe-16Mn-10Al-0.86C-5Ni high specific strength steel, Acta Mater. 109 (2016) 213–222, https://doi.org/10.1016/j.actamat.2016.02.044.
[55] W. Wang, Y. Ma, M. Yang, P. Jiang, F. Yuan, X. Wu, Strain rate effect on tensile behavior for a high specific strength steel: from quasi-static to intermediate strain rates, Metals (Basel) 8 (2018) 11, https://doi.org/10.3390/MET8010011. Page8 (2017) 11.
[56] H. Gao, Y. Huang, Geometrically necessary dislocation and size-dependent plasticity, Scr. Mater. 48 (2003) 113–118, https://doi.org/10.1016/S1359-6462(02)00329-9.
[57] D.A. Hughes, N. Hansen, D.J. Bammann, Geometrically necessary boundaries, incidental dislocation boundaries and geometrically necessary dislocations, Scr. Mater. 48 (2003) 147–153, https://doi.org/10.1016/S1359-6462(02)00358-5.
[58] A. Orlová, M. Pahutová, J. Čadek, Dislocation structure and the effect of stacking-fault energy in high temperature creep of Cu–Al solid solutions, Philos. Mag. 23 (1971) 303–312, https://doi.org/10.1080/14786437108216386.
[59] A. Howie, P.R. Swann, Direct measurements of stacking-fault energies from observations of dislocation nodes, Philos. Mag. 6 (1961) 1215–1226, https://doi.org/10.1080/14786436108243372.
[60] Q.Q. Shao, L.H. Liu, T.W. Fan, D.W. Yuan, J.H. Chen, Effects of solute concentration on the stacking fault energy in copper alloys at finite temperatures, J. Alloys Compd. 726 (2017) 601–607, https://doi.org/10.1016/j.jallcom.2017.07.332.
[61] M. Meyers, K. Chawla, Mechanical Behavior of Materials, Cambridge university press, 2008.
[62] Y.T. Zhu, X.L. Wu, Ductility and plasticity of nanostructured metals: differences and issues, Mater. Today Nano 2 (2018) 15–20, https://doi.org/10.1016/j.mtnano.2018.09.004.
[63] Y.T. Zhu, X.Z. Liao, X.L. Wu, Deformation twinning in nanocrystalline materials, Prog. Mater Sci. 57 (2012) 1–62, https://doi.org/10.1016/j.pmatsci.2011.05.001.
[64] R.Z. Valiev, Y. Estrin, Z. Horita, T.G. Langdon, M.J. Zehetbauer, Y.T. Zhu, Fundamentals of superior properties in bulk NanoSPD materials, Mater. Res. Lett. 4 (2016) 1–21, https://doi.org/10.1080/21663831.2015.1060543.